Electrochemically Induced Metal- vs. Ligand-Based Redox Changes in Mackinawite: Identification of a Fe^{3+}- and Polysulfide-Containing Intermediate

ARTICLE

Electrochemically Induced Metal- vs. Ligand-Based Redox Changes in Mackinawite: Identification of a Fe^{3+}- and Polysulfide-Containing Intermediate

Sebastian A. Sanden,[a,b*] Robert K. Szilagyi,[c*] Yamei Li,[a] Norio Kitadai,[d] Samuel M. Webb,[e] Takaaki Yano,[f] Ryuhei Nakamura,[a,g] Masahiko Hara,[a,b] Shawn E. McGlynn [a,g,h*]

Under anaerobic conditions, ferrous iron reacts with sulfide producing FeS, which can then undergo a temperature, redox potential, and pH dependent maturation process resulting in the formation of oxidized mineral phases, such as gregite or pyrite. A greater understanding of this maturation process holds promise for the development of iron-sulfide catalysts, which are known to promote diverse chemical reactions, such as H^+, CO_2 and NO_3^- reduction processes. Hampering the full realization of the catalytic potential of FeS, however, is an incomplete knowledge of the molecular and redox processess ocurring between mineral and nanoparticulate phases. Here, we investigated the chemical properties of iron-sulfide by cyclic voltammetry, Raman and X-ray absorption spectroscopic techniques. Tracing oxidative maturation pathways by varying electrode potential, nanoparticulate $n(Fe^{2+}S^{2-})_{(s)}$ was found to oxidize to a Fe^{3+} containing FeS phase at -0.5 V vs. Ag/AgCl (pH = 7). In a subsequent oxidation, polysulfides are proposed to give a material that is composed of Fe^{2+}, Fe^{3+}, S^{2-} and polysulfide (S_n^{2-}) species, with its composition described as $Fe^{2+}_{1-3x}Fe^{3+}_{2x}S^{2-}_{1-y}(S_n^{2-})_y$. Thermodynamic properties of model compounds calculated by density functional theory indicate that ligand oxidation occurs in conjunction with structural rearrangements, whereas metal oxidation occurs prior to structural rearrangement. These findings together point to the existence of a metastable FeS phase located at the intersection of a metal-based oxidation path between FeS and greigite ($Fe^{2+}Fe_2^{3+}S_4^{2-}$) and a ligand-based oxidation path between FeS and pyrite ($Fe^{2+}S_2^{2-}$).

Introduction

Iron(II) sulfide is widely encountered in anoxic environments, such as sulfide rich sediments and deep-sea hydrothermal vents.[1,2] In catalysis research, iron-sulfide minerals are valuable low cost alternatives to those involving precious metals.[3,4] Stemming from the catalytic ability of iron sulfides to reduce H^+, CO_2, and NO_3^-, and the widespread observation of iron-sulfur clusters as catalysts and electron mediators in biology, the mineral phases and their surface chemistry are also of high interest in origin of life studies. [5–16]

[a.] Earth Life Science Institute, Tokyo Institute of Technology
2-21-1 IE-1 Ookayama, Meguro, Tokyo 152-8550, Japan.
[b.] School of Materials and Chemical Technology, Tokyo Institute of Technology
4259 G1-7 Nagatsuta, Midori-ku, Yokohama, Kanagawa 226-8502, Japan.
[c.] Department of Chemistry and Biochemistry, Montana State University, Bozeman, MT 59717, USA
[d.] Super-cutting-edge Grand and Advanced Research (SUGAR) Program, Institute for Extra-cutting edge Science and Technology Avant-garde Research (X-star), Japan Agency for Marine-Earth Science and Technology (JAMSTEC), 2-15 Natsushima-cho, Yokosuka 237-0061, Japan
[e.] Stanford Synchrotron Radiation Lightsource, SLAC National Accelerator Laboratory, 2575 Sand Hill Road, Menlo Park, CA 94025, USA
[f.] Institute of Post-LED Photonics, Tokushima University, Minami-Jyosanjima, Tokushima 770-8506, Japan
[g.] Center for Sustainable Resource Science, RIKEN
2-1 Hirosawa. Wako, Saitama 351-0198, Japan.
[h.] Blue Marble Space Institute of Science, Seattle, Washington 98154, USA
* Corresponding authors: sanden@elsi.jp, szilagyi@montana.edu, mcglynn@elsi.jp
Electronic Supplementary Information (ESI) available. See DOI: 10.1039/x0xx00000x

Iron sulfide precipitates undergo a maturation process during which crystallinity, redox state, and molecular stoichiometry may vary.[17,18] In the most reduced form, $Fe^{2+}S^{2-}$ ranges from $n(Fe^{2+}S^{2-})_{(aq)}$ colloidal nanoparticles (with n<150) to precipitated iron(II) sulfide (n>150), which we describe as mackinawite-like nanoparticles $n(Fe^{2+}S^{2-})_{(s)}$.[19] Below pH 4.5, $n(Fe^{2+}S^{2-})_{(aq)}$ also persists as an electroactive, colloidal species with a particle size of ca. 2 nm (referred to as $FeS_{(nano)}$), which represents an intermediate in the formation of crystalline mackinawite ($FeS_{(m)}$) at circumneutral pH.[20] The oxidative phase transformations of $Fe^{2+}S^{2-}$ to pyrite ($Fe^{2+}S_2^{2-}$) and greigite ($Fe^{2+}Fe_2^{3+}S_4$) are complex; depending on the locus of redox chemistry, the oxidation may be ferrous iron or sulfide ligand centered, forming ferric iron or polysulfides, respectively.[17] The importance of understanding these transitions in catalysis research is highlighted by work showing that a greigite working electrode produced C_2 and C_3 compounds from CO_2 when the potential was cycled between -1 and 0 V vs. Ag/AgCl, but not when a constant potential of -1 V was applied.[21] From a perspective of Earth history, the FeS maturation sequence and production of polysulfides are relevant to understanding the preservation of biosignatures, through the sulfidization of organic material by substitution reactions with polysulfides and subsequent burial in marine sediments.[22–24]

Figure 1 depicts an overview of different mineral phases produced by the oxidation of nanoparticulate or crystalline $FeS_{(m)}$. Except for the production of pyrite from ferrous iron and polysulfide ions, most reactions are too slow to be readily observed on short experimental
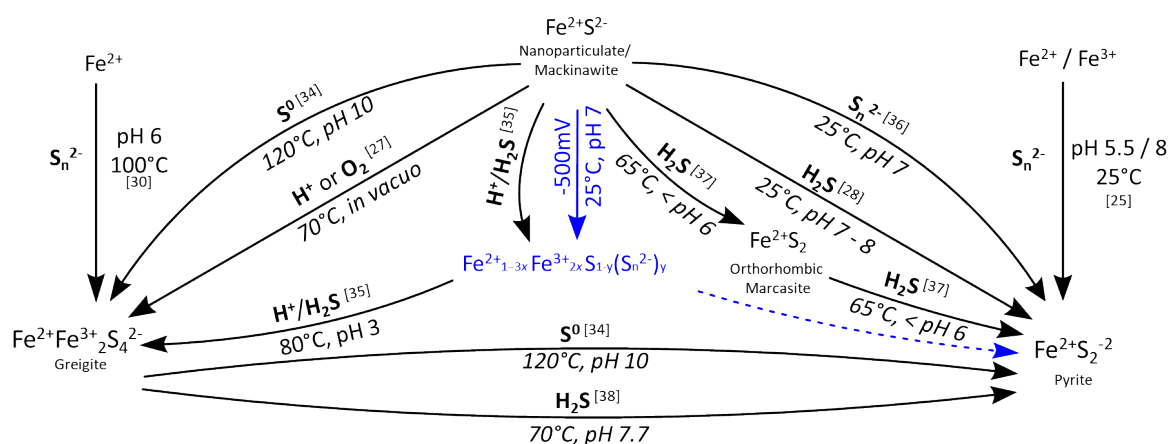
Figure 1, Schematic overview of the known oxidation pathways of iron(II) sulfide/mackinawite to greigite, marcasite and pyrite in aqueous solution. The oxidants employed or assumed in the respective reaction (and along with literature references) are displayed in bold; the pH and temperature of the reaction conditions are indicated below the oxidants. Indicated in blue is the reaction studied in the given work, in which an iron sulfide phase (previously termed ferric iron containing mackinawite[35]) was produced using an indium tin oxide electrode at -0.5 V vs. Ag/AgCl, pH 7. For a detailed review of mineral transformations of FeS, including higher temperatures, see reference 17.

time scales at room temperature.[25,26] When $Fe^{2+}S^{2-}$ is oxidized to greigite (Fe_3S_4), marcasite, or pyrite (FeS_2), a two electron oxidation process takes place involving either H_2S or S^0 as an oxidant that favours the oxidation of Fe^{2+} at elevated temperatures ($\geq 70°C$) or S^{2-} at room temperature.[27–29] Furthermore, polysulfides can act as an oxidant for $Fe^{2+}_{(aq)}$ at elevated temperatures leading to the formation of greigite.[30] Moreover, $n(Fe^{2+}S^{2-})_{(s)}$ has been implicated to form a soluble iron polysulfide complex or cluster that precipitates slowly as pyrite forms under ambient conditions.[25,26] To date, only a reaction kinetics model of pyrite formation from $Fe^{2+}S^{2-}$ and polarographic data hint the existence of an intermediate in the form of a complex or cluster ($[Fe-S]_x (S_n^{2-})_y$).[26]

During the oxidation of mackinawite ($FeS_{(m)}$) to greigite by $Fe^{3+}_{(aq)}$ or O_2, a Fe^{3+} containing phase has been detected by Raman and Mössbauer spectroscopy.[31,32] This FeS phase was previously undetected likely due to a lack of X-ray diffraction patterns distinguishable from mackinawite owing to poor crystallinity.[33,34] Based on Mössbauer spectra and Fe K-edge X-ray absorption near-edge structure (XANES) analysis, the Fe^{3+} content of this material was estimated to be up to 20 mol% of the total iron content and it was termed Fe^{3+} containing mackinawite, with a tentative chemical formula of $Fe^{2+}_{1-3x}Fe^{3+}_{2x}S^{2-}$ (x < 0.1).[33,35] Electrochemical access to this Fe^{3+} containing mackinawite, as well as control over the formation of polysulfides, could allow selective synthesis of pyrite and greigite. Since these minerals promote different reactions, selective synthesis via controlled ligand– versus metal–based oxidation – as well as access to their intermediates – would be valuable for industrial applications and for understanding the nature of geochemical transformations.

Here, we investigated these oxidative phase transitions by performing cyclic voltammetry on $n(Fe^{2+}S^{2-})_{(s)}$, which was freshly precipitated on a solid-state indium tin oxide electrode (ITO). The observed redox reactions suggested from the voltammetric signals were analyzed by ex-situ sulfur K-edge X-ray absorption near-edge

spectroscopy (XANES) and Raman spectroscopy. Computational models for plausible FeS complexes, clusters, and FeS nanoparticles were generated to compare and contrast various compositions and formation mechanisms of Fe^{3+} containing mackinawite.

Experimental Section

Iron(II) sulfide was freshly precipitated from an equimolar amount of iron(II) chloride tetrahydrate (99.99%, Sigma) and sodium sulfide nonahydrate (99.99%, Sigma) dissolved in Milli-Q water (18.2 MΩ, Millipore Ltd.), which was deaerated by stirring the vial uncapped in a COY glove box overnight prior to usage. All solutions were prepared, and manipulations performed in a plastic sided glove box filled with an atmosphere of 4% H_2 and 96% N_2 and deoxygenated with palladium catalysts (COY).

The cyclic voltammograms of $n(Fe^{2+}S^{2-})_{(s)}$ samples were measured with a HZ-7000 potentiostat (Hokuto Denko) at a scanning speed of 10 mV s^{-1} and all electrode potentials are given here in reference to Ag/AgCl (in a saturated KCl solution). For these voltammograms, equal volumes (400 µl) of 200 mM $FeCl_{2(aq)}$ and 200 mM $Na_2S_{(aq)}$ were reacted for 10 min on top of an ITO electrode with a surface area of about 11.3 cm^2 and then diluted to a 7 ml volume with a K_2HPO_4 buffer solution (200 mM, pH 7.0). For a control experiment containing polysulfides, sodium polysulfides (Na_2S_n) were first prepared by dissolving 0.7 mmol of Na_2S and adding 2 mmol sublimed elemental sulfur (99%, Wako) in 5 ml Milli-Q water, with heating at 70 °C for 24h, before being dried in vacuo in a 4% H_2/N_2 environment using a dry vacuum pump. As a rough estimate of the molecular weight of Na_2S_n, the molecular weights of the dominant polysulfide species of Na_2S_2 up to Na_2S_5 were averaged (158 g/mol).[39] 5.7 mM $Na_2S_{n(aq)}$ was added to 11.4 mM $n(Fe^{2+}S^{2-})_{(s)}$ at an approximate stoichiometric ratio of 2:2:1 for $Fe^{2+}:S^{2-}:S_n^{2-}$. For the voltammograms of experiments that did not contain iron, 0.5 mM of the prepared $Na_2S_{(aq)}$ and 0.5 mM $Na_2S_{n(aq)}$ were dissolved in 100 mM

K$_2$HPO$_4$ buffer (pH 7) shortly before the analysis as to minimize degassing of H$_2$S.

For the S K-edge XANES samples, batches of 20 μl of 100 mM FeCl$_{2(aq)}$ and Na$_2$S$_{(aq)}$ were reacted first and then diluted with a 100 mM Tris HCl (Sigma) buffer at pH 7.0 to a final volume of 5 ml on top of an indium tin oxide electrode (ITO). An Ag/AgCl electrode in saturated KCl was used as a reference electrode in a conventional triple-electrode assembly and the electrode potential controlled via an Ivium Technologies *Compactstat.h* potentiostat. After applying the desired electrode potentials to the samples, the supernatant was removed, and the precipitate was collected by pipet and dried at 60°C on a hot plate overnight inside the glovebox. As controls for the expected products, 17.6 μmol n(Fe^{2+}S^{2-})$_{(s)}$ precipitate was also combined with either 1 mM iron(III) chloride hexahydrate (97%, Sigma) or 1 mM potassium polysulfide (≥42%, Sigma) (molar ratio ~1:2.5 Fe^{2+}S^{2-} to Fe^{3+} or S$_n$$^{2-}$) shortly after precipitation of the material. The dry powders were mounted between a coverslip and a 2 mm × 2 mm and 200 nm thickness silicon nitride window (Norcada) and sealed with a cyanoacrylate-based glue. Samples were sealed in two plastic bags prior to the transfer from the COY glovebox to the beamline.

Sulfur K-edge XANES spectra were recorded at beamline 14-3 of the Stanford Synchrotron Radiation Lightsource (SSRL). The incident x-ray energy was obtained using a Si(111) double crystal monochromator with the Stanford Positron Electron Accelerating Ring (SPEAR) storage ring containing 500 mA at 3.0 GeV in top-off mode. The fluorescence lines of the elements of interest were monitored using a silicon drift Vortex detector (Hitachi) using *Xspress3* pulse processing electronics (Quantum Detectors). The sample area was purged with helium gas. Calibration of the X-rays was accomplished by setting the pre-edge peak of sodium thiosulfate at 2472.02 eV. Suitable spectra from three detector channels were selected using the SIXPACK software package.[40] The normalization of the spectra was performed using ATHENA.[41]

Raman spectra were measured for n(Fe^{2+}S^{2-})$_{(s)}$ samples that were prepared as described above for the electrochemical measurements, but with an additional drying step in vacuo in order to minimize scattering due to water. The dry powder was placed in an airtight environmental sample cell (LIBcell, Nanophoton) and analyzed by a Raman laser (532 nm) scanning microscope from Nanophoton with a 20× objective in point measurement mode. Each sample was illuminated for 10s, for which over 200 scattering spectra were collected to generate an averaged spectrum. The spectrum was calibrated against crystalline silicon at 521 cm^{-1} and the laser power was set to be between 1.5–2.5 mW to ensure that the samples were not exposed to excessive heating during the measurement. The spectra of n(Fe^{2+}S^{2-})$_{(s)}$ samples utilized in electrochemical experiments were recorded at a minimum of 3 different locations to assure reproducibility. In this process, only spectra with the same number of peaks and peak positions were averaged; otherwise, they were displayed as individual spectra. As a chemical reference for the possible oxidation products (such as pyrite and greigite), ca. 0.5 mmol Na$_2$S$_{n(aq)}$ and 0.1 mmol FeCl$_{2(aq)}$ were reacted in 1 ml Milli-Q water at room temperature for three days prior to analysis.

Density Functional Theory (DFT) calculations were performed using a hybrid, gradient corrected Becke-Perdew86 (BP86) functional with 5% Hartree-Fock exchange in combination with a triple-ζ quality basis set[42] def2-TZVP as implemented in Gaussian16 Rev.C.01.[43–45] This functional was selected in order to obtain an experimentally sound description for the electronic and geometric structures of the FeS system. Given the studied aqueous FeS systems and the presence of H$_2$O after drying of FeS samples, the computational models were embedded in a polarizable solvent continuum (SMD).[46] The charge distribution was computed using Hirshfeld population analysis method.[47] Atomic spin density values were obtained from Mulliken population analysis.[48] Clusters and complexes are noted as ^{M}[X]^Z, where M is the spin multiplicity (2S+1) and Z the molecular charge of the relevant species X.

Results and Discussion

Voltammetry of n(Fe^{2+}S^{2-})$_{(s)}$: Iron-sulfur redox and the formation of polysulfides

Starting from an open circuit potential of -0.56 V for freshly precipitated n(Fe^{2+}S^{2-})$_{(s)}$, the first voltammetric scan was directed toward lower potentials up to -0.80 V (Figure 2a). The large cathodic current reaching a maximum at -0.8 V was observed in all voltametric experiments and is attributed to proton reduction producing H$_2$. The first anodic peak (A1) was observed at -0.39 V (Figure 2a), a smaller second peak at -0.19 V (A2), and a third at -0.05 V (A3).

Similar to A2, FeCl$_{3(aq)}$ in a 200 mM K$_2$HPO$_4$ pH 7 buffer showed a redox wave with an anodic peak at -0.18 V (Figure 2a, red trace). Additionally, the cathodic sweep showed a peak for both n(Fe^{2+}S^{2-})$_{(s)}$ and FeCl$_{3(aq)}$ at -0.41 V (C1). Since [Fe(OH$_2$)$_6$]$^{2+}$$_{(aq)}$ co-exists with n(Fe^{2+}S^{2-})$_{(s)}$ despite FeCl$_{2(aq)}$ and Na$_2$S$_{(aq)}$ being reacted in 1:1 stoichiometries,[49] A2 and C1 are attributed to the reversible redox reaction of aqueous Fe^{2+}/Fe^{3+} at pH 7:

A2 / C1   [Fe(OH$_2$)$_6$]$^{2+}$+ H$_2$O ⇋ [Fe(OH)(OH$_2$)$_5$]$^{2+}$ + H$_3$O$^+$ + 1e$^-$
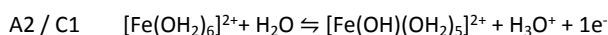
Adding S$_n$$^{2-}$ to n(FeS)$_{(s)}$ in a 1:2 stoichiometric ratio significantly changed the voltammogram. The current for peak A1 decreased (Figure 2b), which coincided with the precipitate becoming a black suspension. Solubilization of n(Fe^{2+}S^{2-})$_{(s)}$ was observed previously with polysulfide addition at pH 7, and [Fe-S]$_x$ (S$_n$$^{2-}$)$_y$ complexes or clusters were proposed to be the reaction product exhibiting an anodic peak.[25] Contrary to this, in our samples, no new anodic peak was observed. A decreased current for A1 might be attributed to diminished contact with the electrode upon solubilization of n(Fe^{2+}S^{2-})$_{(s)}$ or could also be attributed to a decreased electroactivity due to the presence of a high concentration of negative charged polysulfide species interfering with electronic contact with the ITO electrode.
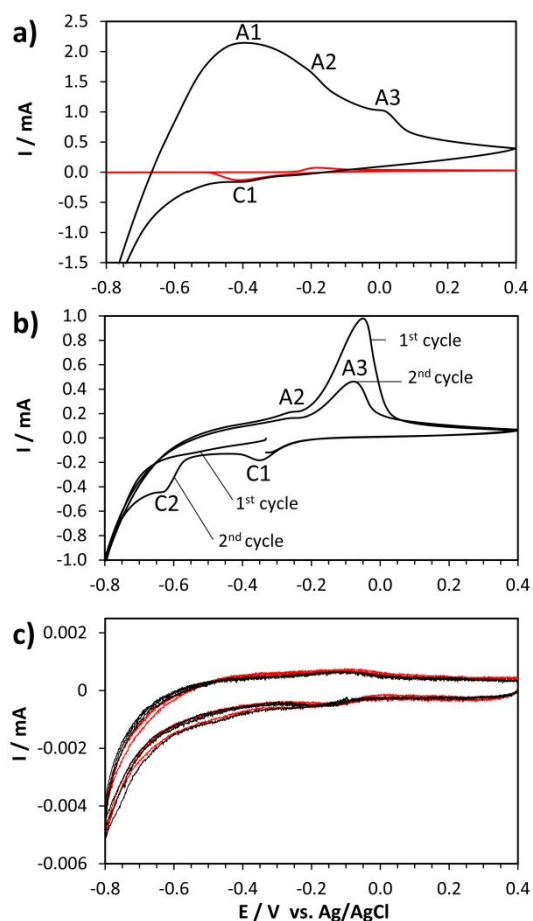
Figure 2, *Cyclic voltammograms of a) the first cycle of 11.4 mM $n(Fe^{2+}S^{2-})_{(s)}$ (formed from equimolar $Fe^{2+}_{(aq)}$ and $S^{2-}_{(aq)}$ (black trace) and 11.4 mM $FeCl_3$ in red (for which the second voltammetric cycle is shown) and b) 5.7 mM $Na_2S_{n(aq)}$ and 11.4 mM $n(Fe^{2+}S^{2-})_{(s)}$ in 200 mM K_2HPO_4 (pH 7), which shows both the first and second voltammetric cycle. Panel c) depicts a voltammetric sweep of 0.5 mM $Na_2S_{(aq)}$ (red) and ca. 0.5 mM $Na_2S_{n(aq)}$ in a 100 mM K_2HPO_4 buffer (pH 7) (black). The scanning speed was 10 mV s^{-1} and the open circuit potential was the starting point for the potential sweep.*

The addition of S_n^{2-} led to peak A3 exhibiting the highest anodic current at about -0.05 V (Figure 2b). This reaction is proposed to be the oxidation of polysulfides to elemental sulfur according to the following reaction:

A3 $\qquad\qquad S_n^{2-}_{(aq)} \rightarrow n/8\ S_{8(s)} + 2\ e^-$

Based on the free energies of formation for polysulfides[39] and rhombic elemental sulfur[50] in aqueous solution, the oxidation of the most abundant (deprotonated) $S_5^{2-}_{(aq)}$ species has a standard redox potential of -0.54 V vs. Ag/AgCl, but an oxidation potential of ~0 V (pH 6.8) similar to peak A3 was reported for polysulfide oxidation on Au electrodes.[51]

After an anodic scan, another cathodic peak (C2) appeared at -0.63 V for $n(Fe^{2+}S^{2-})_{(s)}$ in the presence of $S_n^{2-}_{(aq)}$ (Figure 2b). The standard redox potentials of the S_8/HS$^-$ and the S_2^{2-}/HS$^-$ redox pairs are -0.34 V and -0.32 V Ag/AgCl (pH 7) respectively.[32] As peak C2 is only observed
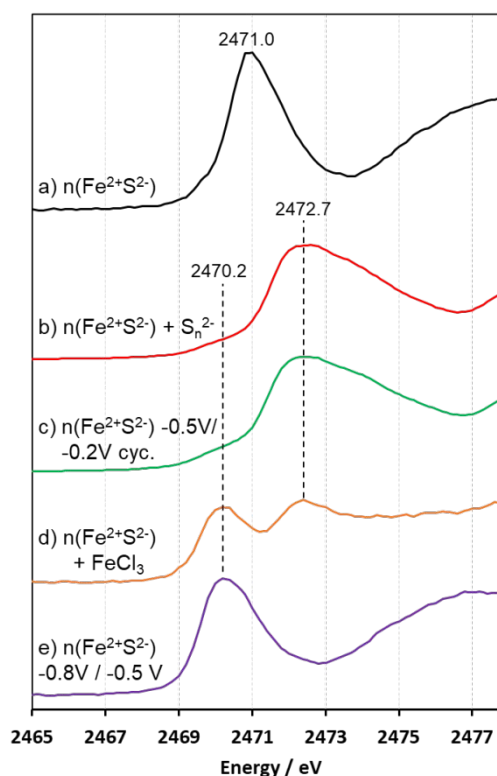

Figure 3, *Normalized sulfur K-edge X-ray near-edge absorbance spectra of untreated $n(Fe^{2+}S^{2-})_{(s)}$ (a), $n(Fe^{2+}S^{2-})_{(s)}$ to which $Na_2S_{n(aq)}$ was added (b) and $n(Fe^{2+}S^{2-})_{(s)}$ cycled between -0.5V and -0.2V (c). Samples for $n(Fe^{2+}S^{2-})_{(s)}$ incorporating Fe^{3+} were obtained by the addition of $FeCl_{3(aq)}$ to $n(Fe^{2+}S^{2-})_{(s)}$, depicted in trace (d), or electrochemical oxidation of $n(Fe^{2+}S^{2-})_{(s)}$ at -0.5 V (e). The energy scale is expressed in electron volts and was calibrated against the first pre-edge feature of sodium thiosulfate at 2472.02 eV.*

on the second scan, after the putative deposition of elemental sulfur at peak A3, the reduction of S_8 likely proceeds as:

C2 $\qquad n/8\ S_8^0_{(aq)} + n\ H_3O^+_{(aq)} + 2n\ e^- \rightarrow n\ HS^-_{(aq)} + n\ H_2O_{(l)}$
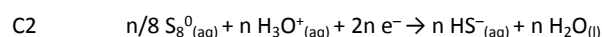
Importantly, no oxidation reaction occurs on the ITO electrode using solely $Na_2S_{(aq)}$ or $Na_2S_{n(aq)}$ in a phosphate buffer (Figure 2c). Thus, none of the above assigned peaks for $n(Fe^{2+}S^{2-})_{(s)}$ with or without polysulfides can be attributed to the underpotential deposition of sulfide on the electrode surface, as reported for Au electrodes.[51] The suppression of sulfide oxidation on ITO has been reported earlier when a phosphate buffer was used. It was hypothesized that $H_2PO_4^-$/HPO_4^{2-} anions hinder the diffusion of $HS^-_{(aq)}$ to the electrode surface.[52] This demonstrates that the presence of iron ions is necessary to render sulfide and polysulfides electroactive on ITO in a 100 mM phosphate buffer, and suggests that the oxidation of iron-bound sulfides to polysulfides might also feature metal-centered redox changes.

XANES spectroscopy: Iron oxidation precedes sulfur oxidation

To gain more insight into the iron and sulfur redox changes occurring on the electrode, XANES spectroscopic measurements were performed with samples oxidized at electrode potentials
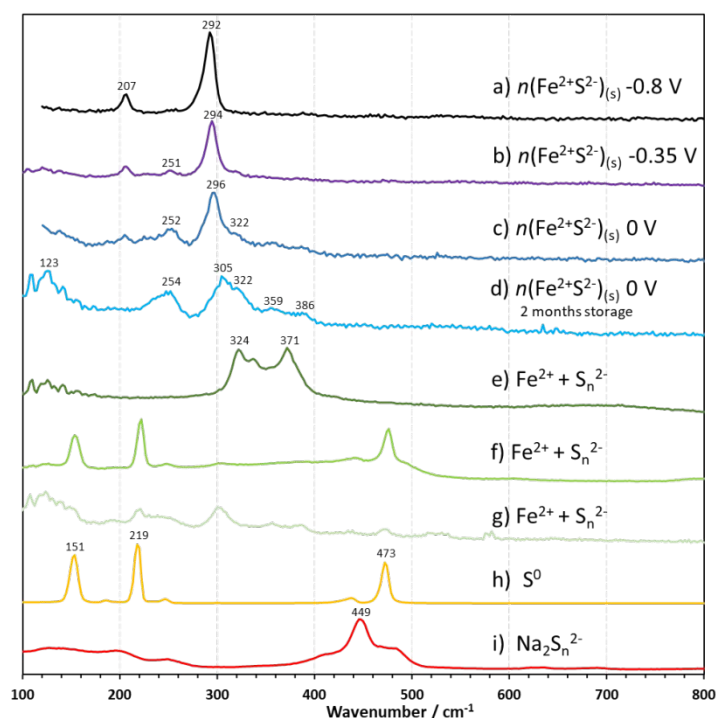
Figure 4, *Raman spectra of electrochemically treated* $n(Fe^{2+}S^{2-})_{(s)}$, *a reaction between ferrous iron and polysulfides, and reference materials. Spectra a) to c) depict* $n(Fe^{2+}S^{2-})_{(s)}$ *with applied potentials of -0.8 V (a), -0.35 V (b), 0 V (c) and* $n(Fe^{2+}S^{2-})_{(s)}$ *to which an electrode potential of 0 V vs. Ag/AgCl was applied and subsequently stored in an anaerobic environment 2 months prior to the analysis (d). Dry, heterogeneous material obtained from a reaction of* $FeCl_{2(aq)}$ *and* $Na_2S_{n(aq)}$ *is depicted in e), f) and g,) sublimed elemental sulfur in h) and a preparation of* $Na_2S_{(s)}$ *under anaerobic conditions is displayed in i). The Raman peak positions for the electrochemical experiments are presented in Figure S2 (ESI).*

corresponding to the observed anodic peaks. Trace a) in Figure 3 depicts the S K-edge XANES spectrum of untreated $n(Fe^{2+}S^{2-})_{(s)}$ with its main edge peak located at 2471.0 eV. To obtain samples of $n(FeS)_{(s)}$ that incorporate Fe^{3+} and S_n^{2-} ions, either $Na_2S_{n(aq)}$ or $FeCl_{3(aq)}$ were added to $n(Fe^{2+}S^{2-})_{(s)}$ in a molar ratio 1:2.5 $Fe^{2+}S^{2-}$ to Fe^{3+} or S_n^{2-} (trace b and d). Figure 3c displays the S K-edge absorbance of $n(Fe^{2+}S^{2-})_{(s)}$, which was cycled between -0.5 V and -0.2 V for 3.5h to accumulate polysulfides between the potentials of their oxidation to sulfur (peak A3) and the onset of the large cathodic current at -0.5 V. Both the control experiment of $n(Fe^{2+}S^{2-})_{(s)}$ with added $S_n^{2-}{}_{(aq)}$ (Figure 3b) and the electrochemical experiment (Figure 3c) show the main edge peak at 2472.7 eV, which is also observed for $S_{8(s)}$ (ESI, Figure S1, trace i).

The weak and broad pre-edge feature at 2470.2 eV may correspond to the presence of small amounts of polysulfides, as these features arise from the 1s to 3p-based, S–S σ* transitions of the terminal and internal sulfur atoms at 2472.7 eV, respectively.[53] However, these pre-edge features can also arise from alternative species, such as S-radicals, cation bound terminal S atoms of persulfides (i.e. vacant Li 2s/2p mixing with occupied S 3p orbitals)[54] or covalent Fe-S bonding (vacant Fe 3d mixing with occupied S 3p orbitals).[55] The main transition at 2472.7 eV and the pre-edge feature at 2470.2 eV could thus correspond to either polysulfides or elemental sulfur and covalent Fe^{3+}–S^{2-} bonds.

To determine the changes of the electronic environment and redox state of sulfide at voltametric peak A1, $n(Fe^{2+}S^{2-})_{(s)}$ was exposed to

-0.8 V for 1.5h (following the scan direction of the voltametric experiments) and then stabilized at -0.5 V for 2h (Figure 3e). The main edge of the electrochemical experiment at 2470.2 eV coincides with the Fe^{3+} containing $n(Fe^{2+}S^{2-})_{(s)}$ control sample (Figure 3d), whereas the sulfur K-edge peak of untreated $n(Fe^{2+}S^{2-})_{(s)}$ can be found 0.8 eV higher (Figure 3a). The shift to lower energies for Fe^{3+} bound sulfides is likely due to the higher nuclear charge of ferric iron that lowers the Fe d-manifold relative to ferrous iron, as can be clearly followed in the S K-edge XANES spectra of metal thiolate complexes and [4Fe-4S] clusters.[55,56] The anodic current A1 can thus be associated with the oxidation of $n(Fe^{2+}S^{2-})_{(s)}$ to a ferric iron bound to sulfide, although quantification is prohibited since both the rising-edge feature of terminal polysulfides and pre-edge ferric sulfide show a peak at 2470.2 eV.[54] The absence of a signal corresponding to S_8^0 after applying -0.5V to $n(Fe^{2+}S^{2-})_{(s)}$ suggests that the oxidation of iron precedes the oxidation of sulfide.

Raman spectroscopy: An oxidative progression to ferric iron containing mackinawite

Raman spectra for $n(Fe^{2+}S^{2-})_{(s)}$ were measured after applying a potential of -0.8 V, -0.35 V, or 0 V for 48h (Figure 4, a,b and c). The sample exposed to 0 V was also reanalyzed after 2 months storage inside a glovebox maintaining an O_2 level of below the detection limit (≤ ~20ppm). From the -0.8 V preparation, the $n(Fe^{2+}S^{2-})_{(s)}$ precipitate exhibited the characteristic vibrational modes of mackinawite at 207 cm^{-1} (a_{1g} mode) and 292 cm^{-1} (b_{1g} mode) (Figure 4a).[35,57] Exposure to a potential of -0.35 V produced new Raman bands at 251 cm^{-1} and at
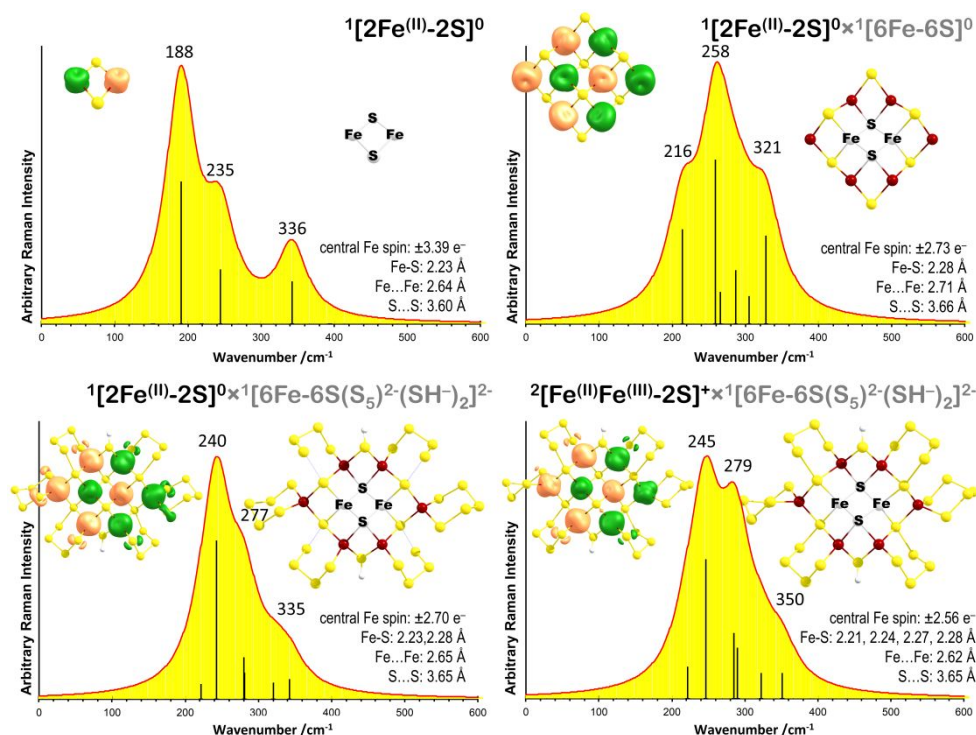
Figure 5, *Simulated Raman spectra for the ^{1}[2Fe-2S]^0 rhomb (top left), the ^{1}[8Fe-8S]^0 cluster or core ^{1}[2Fe-2S]^0 rhombs embedded in a ring of ^{1}[6Fe-6S]^0 as a model for 8(FeS)$_{(aq)}$ nanoparticles (top right), and the persulfide and bisulfide terminated 8(FeS)$_{(aq)}$ nanoparticle model in an all ferrous (bottom left) and one-electron oxidized form (bottom right) with selected intramolecular distances at B(5%HF)P86/def2TZP/SMD(water) level of theory. Interatomic distances, atomic spin densities, and spin density contour plots (orange/green are positive and negative spin contours at 0.01 e^{-2}/Å^3 levels), are provided to illustrate the electronic and geometric structural differences among the models.*

322 cm^{-1} (Figure 4b), which were both previously assigned to Fe^{3+} containing mackinawite.[32,35]

The spectra acquired at 0 V for the freshly precipitated and aged n(Fe^{2+}S^{2-})$_{(s)}$ display broad peaks that are distinct from mackinawite at ~253, 322, and 350-360 cm^{-1} (Figure 4c, d). These peaks are consistent with the previously reported Raman bands for Fe^{3+} containing mackinawite.[35] The Raman band at 359 cm^{-1} detected for aged n(Fe^{2+}S^{2-})$_{(s)}$ at 0 V could also correspond to the highest intensity Raman bands of greigite at ~355 and ~365 cm^{-1}, but other vibrational modes (190 and 247cm^{-1}) of this mineral were not observed. The appearance of the additional Raman band at 359 cm^{-1}, as well as an increase in peak intensities (relative to the b$_{1g}$ mode of mackinawite near 295 cm^{-1}) suggests an oxidative progression from -0.35 V to 0 V. The Fe^{2+}S^{2-} b$_{1g}$ normal mode shifted from 292 cm^{-1} at -0.8 V to 297 cm^{-1} at 0 V, and up to 305 cm^{-1} after 2 months storage under anaerobic conditions. This blue shift of the normal mode was previously attributed to the presence of ferric iron[35] and is also consistent with an oxidative progression at more positive electrode potentials. This interpretation that the shift of the ~295 cm^{-1} feature is related to the presence of Fe^{3+} ion, is affirmed here based on the example of oxidized [8Fe-8S] cluster models derived from DFT, which are discussed below (c.f. Figures 5 and 6).

As the oxidation of sulfide to polysulfides was suggested to occur in n(Fe^{2+}S^{2-})$_{(s)}$ during our cyclic voltammetry experiments (A3 of Figure 2a, b), a complementary reference material was prepared by reacting Na$_2$S$_{n(aq)}$ with FeCl$_{2(aq)}$. This experiment was found to give a

heterogeneous material, of which three representative spectra are shown in Figure 4, traces e, f, and g. Spectrum e) shows peaks characteristic for pyrite at 324 and 374 cm^{-1} and also an additional peak at 337 cm^{-1} of unknown origin. The Raman spectrum of elemental sulfur (Figure 4, trace h) displays peaks at 151, 219, and 473 cm^{-1}, which can also be found as minor peaks in spectrum g) in Figure 4. This indicates the formation of elemental sulfur upon addition of polysulfides to ferrous iron. The high intensity peak at 302 cm^{-1} in spectrum g) is assumed to originate from n(Fe^{2+}S^{2-})$_{(s)}$, which, together with the presence of elemental sulfur, matches earlier findings that the first products formed during the reaction of S$_n^{2-}$$_{(aq)}$ and Fe^{2+}$_{(aq)}$ are n(Fe^{2+}S^{2-})$_{(s)}$ and S^0$_{(s)}$.[17] Neither the Fe^{2+} + S$_n^{2-}$ reference material nor electrochemically oxidized n(Fe^{2+}S^{2-})$_{(s)}$ exhibit the highest intensity Raman band at 449 cm^{-1} found for Na$_2$S$_{n(s)}$ (Figure 4i), which suggests the absence of non-coordinated, long chain polysulfides in our samples. Spectra d), e) and g) in Figure 4 exhibit the same closely spaced peaks at 94, 110, 119, 126, 134 and 143 cm^{-1} for both the electrochemical experiment at 0 V and the reaction of Fe^{2+} + S$_n^{2-}$. These features are proposed here to arise from the coordination of polysulfide species to Fe^{2+} and Fe^{3+}, as discussed below for the computed resonance frequencies of metal bound persulfides and polysulfides.

Vibrational analysis of n(Fe^{2+}S^{2-})$_{(aq)}$ nanoparticle models (n=8)

The origin of the observed Raman peaks during electrochemical oxidation was investigated by using DFT-based vibrational analyses. The literature often cites the [2Fe-2S] rhomb as the characteristic
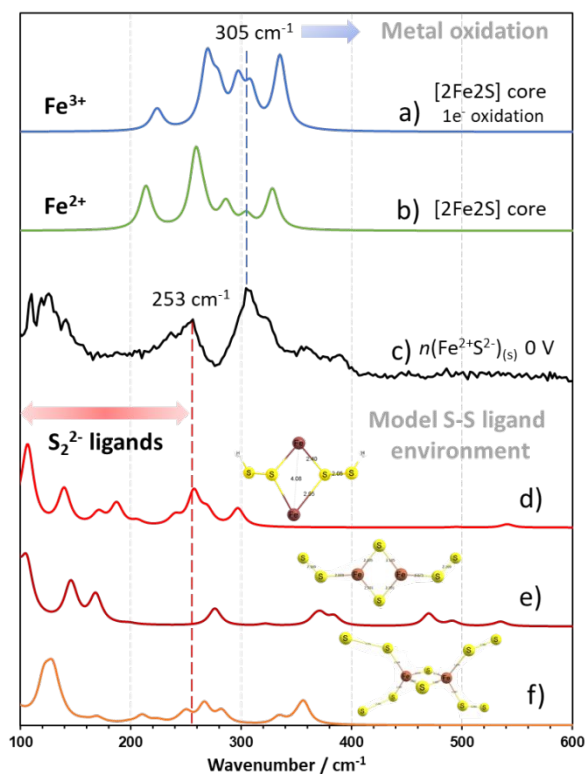
Figure 6, *Simulated Raman spectra of [2Fe-2S] cores from FeS nanoparticles and model persulfide ligand environments on the example of [2Fe-2S] clusters, in comparison to* $n(Fe^{2+}S^{2-})_{(s)}$ *oxidized at 0 V. Spectra a) and b) correspond to core extracted [2Fe-2S] rhombs, where a) depicts the blue-shifted Raman bands of a 1e⁻ oxidized* $8(FeS)_{(aq)}$ *particle and b) the non-oxidized, neutral charge* $8(FeS)_{(aq)}$ *particle. Raman spectrum c) depicts the measured spectrum of* $n(Fe^{2+}S^{2-})_{(s)}$ *oxidized at 0 V, which was stored anaerobically for 2 months. Spectra d) to f) show the vibrational modes of persulfide ligated [2Fe-2S] clusters, where d) corresponds to* $^2[2Fe–(SSH)_2]^{3+}$*, e) to* $^1\{[2Fe-2S](S_2^{2-})_2\}^{4-}$ *and f) to* $^1\{[2Fe-2S](S_2^{2-})_4\}^{8-}$*.*

structural unit of mackinawite.[17] In order to correlate spectral and electrochemical features to composition and structure, we first modelled the metal- and ligand-based redox changes of an isolated [2Fe-2S] rhomb. The changes in the Fe-S bonding and consequences to the Raman active vibrational modes are summarized in Table S1 (ESI) and discussed in the SI Appendix.

Building on these computational models, we derived [2Fe-2S] core-only Raman active modes to eliminate the interfering peaks from peripheral dangling ligands encountered when the [2Fe-2S] unit is part of a larger molecule. This focus on the core is warranted because the contribution of dangling ligands to the experimentally observed Raman peaks is negligible due to their low surface concentrations relative to the bulk of the nanoparticle surface. Moreover, the polarizable continuum embedded [8Fe-8S] cluster is an experimentally relevant species for mackinawite-like nanoparticle formation in the smaller nucleation domain.[19] The [8Fe-8S] cluster is the smallest model which can provide a chemical representation of a central [2Fe-2S] rhomb embedded in a ring of peripheral 6Fe²⁺ and

$6S^{2-}$ ions, where termination of the [2Fe-2S] rhomb environment completes the tetrahedral and tetragonal pyramidal coordination for the ferrous and sulfide ions, respectively. The core-extracted Raman spectra validate the accuracy of the employed level of theory in predicting Raman spectra by a scaled-quantum mechanical force field (SQM-FF) treatment (see Table S2, ESI).[58,59] Using the experimental Raman peaks of mackinawite, a periodic computational model,[60] and our molecular cluster model we obtain a 94-96% scaling factor and 11-16 cm⁻¹ shift to achieve the best least-square fit to experiment. The SQM-FF parameters cause small changes in the calculated spectra in comparison to the experimentally observed chemical shifts; thus, we did not employ them in our current study.

Figure 5 compares these peripheral chemical environments from the complete absence in [2Fe-2S], through an incomplete [8Fe-8S] model without polysulfides, to a plausible persulfide saturated limit for the formally all ferrous and mixed ferrous/ferric central [2Fe-2S] rhombs. With the exception of the isolated [2Fe-2S] rhomb, the dominance of a 240–280 cm⁻¹ feature is apparent (Figure 5). Structural and electronic perturbations are manifested in the variation of the peak intensity, line-shape, and slight shift of envelop of Raman peaks around 250 cm⁻¹, which is thought to correspond to the first distinct Raman band at ~253 cm⁻¹ observed during the oxidation of $n(Fe^{2+}S^{2-})_{(s)}$ (Figure 4 b, c, d). A 1e⁻ oxidation of the [8Fe-8S] neutral cluster results in a small shift of the Raman peaks to higher wavenumbers as compared to the [2Fe–2S] clusters given that the electron hole delocalizes throughout the entire cluster (see [8Fe–8S)]⁰/⁺ in Table S1, ESI). Importantly, this shift matches the observations that higher applied oxidation potentials cause a shift of the normal mode of $n(Fe^{2+}S^{2-})_{(s)}$ from 294 to 305 cm⁻¹ (Figure 4, traces a-d). With these results, we propose that the experimentally observed intensity increase of the ~253 cm⁻¹ peak is originating from the presence of molecular ferrous iron/sulfide clusters with defects, due to oxidation state change (to nominally ferric iron), or variation in the ligand environment (persulfide, polysulfide, bisulfide versus bridging sulfides). This peak was predicted to be present for the idealized mackinawite periodic structure only at a very low intensity, which may become more prominent due to lattice defects induced by oxidation.[57]

Persulfide and polysulfide ligand environment

In addition to the core-extracted [2Fe-2S] rhombs, smaller [2Fe-2S] clusters with persulfide ligands were also computed to investigate the vibrational modes of iron bound persulfides. FeS clusters with bridging persulfides or terminal persulfide ligands produce several high intensity Raman bands below 253 cm⁻¹, similar to the observed Raman bands in the electrochemical experiments (Figure 6, traces c-f). The $^2[2Fe-(SSH)_2]^{3+}$ cluster also exhibits a vibrational mode at 257 cm⁻¹ (Figure 6d), which is close to the 253 cm⁻¹ peak observed for $n(Fe^{2+}S^{2-})_{(s)}$ at 0 V. The high intensity vibrational modes below 140 cm⁻¹ and near 253 cm⁻¹ were also calculated for hypothetical iron persulfide complexes, which are intended to serve as a model ligand environment for iron bound persulfides (Figure S32–S57, ESI). Based on these observations, the closely spaced Raman peaks below 140 cm⁻¹ in the experimental spectra (Figure 4,
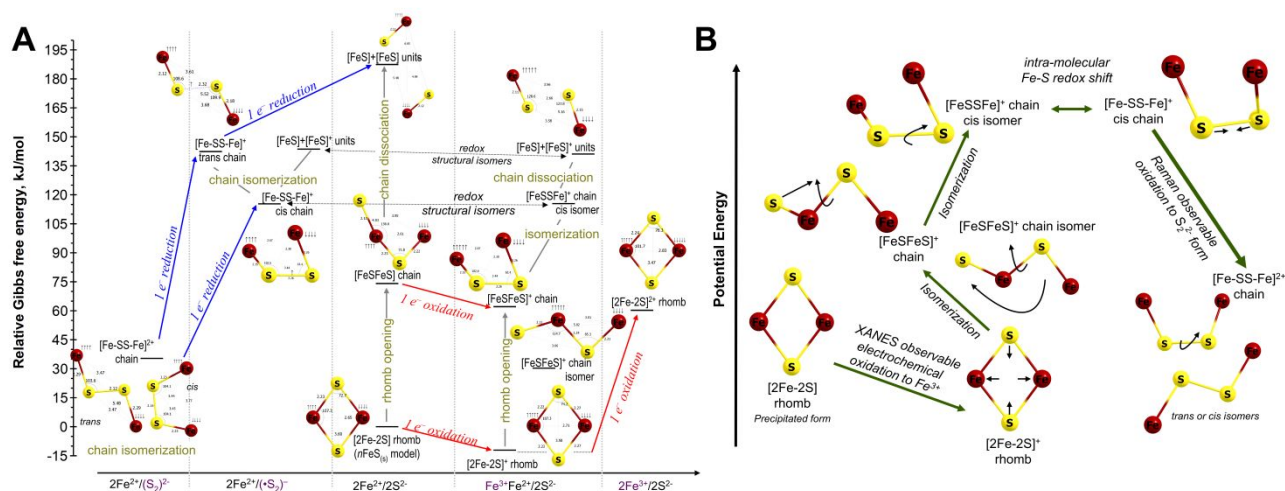
Figure 7, *A) Potential energy surface map of redox processes between the mackinawite-like [2Fe-2S] rhomb (bottom right) and a pyrite-like [Fe-SS-Fe]²⁺ ligand oxidized chain (bottom left) with conserved stoichiometry. Blue and red arrows indicate 1e⁻ reduction and oxidation steps, respectively. Changes in the oxidation state of Fe and S within the models are indicated on the x-axis. Thin, olive green vertical lines mark changes in chemical bonding for isoelectronic, isomeric species with the same metal and ligand redox state. Small black arrows correspond to the number and spin of unpaired electrons. Gibbs energies were estimated at B(5%HF)P86/def2TZVP/PCM (water SMD) level of theory. The electron energy for redox is taken from Ag/AgCl potential +197 mV relative to SHE (4.21 V). B) The FeS transitions that are directly relevant to the work presented here are shown, illustrating a potential pathway between precipitated FeS and pyrite. Precipitated n(Fe²⁺S²⁻)(s) (modeled as a 2(FeS)(aq) rhomb) is electrochemically oxidized, producing a ferric iron containing species observed by XANES. A pathway of isomerizations leads to an intra-molecular redox shift where 2Fe³⁺ oxidizes 2S²⁻ to (S₂)²⁻ (the [Fe-SS-Fe]⁺ cis chain at top right). Subsequent oxidation leads to a pyrite-like Fe-SS-Fe chain with Raman observable polysulfide (S₂²⁻).*

traces d, e, and g), could therefore originate from iron bound persulfides.

The increase in the relative Raman intensities below 140 cm⁻¹ for $n(Fe^{2+}S^{2-})_{(s)}$ from -0.8 V to 0 V (Figure 4) and this analysis corroborates the interpretation of the cyclic voltammetry experiments that polysulfides, and disulfides in particular, are generated through the oxidation of sulfide above -0.5 V.

The synthesis and structural characterization of an [2Fe–2S] cluster with two pentasulfide ligands has been reported.[61] The here calculated equilibrium structure is in good agreement with the measured structure and has a root mean square deviation in bond lengths and bond angles of 0.018 Å and 0.92°, respectively. The vibrational normal modes were calculated and highly Raman active polysulfide stretching modes above 400 cm⁻¹ were observed for the nominally ferrous iron containing $^1[2Fe^{2+}-2(S_5^{2-})]^{4-}$ (Figure S13, ESI). The measured Raman spectrum of $Na_2S_{n(s)}$ exhibits similar high intensity Raman band at 449 cm⁻¹ (Figure 4 e), corresponding to internal S-S stretching modes of polysulfides.[62] Because no Raman bands were observed > 400 cm⁻¹ in any of the studied electrode potentials, pentasulfide clusters and non-iron bound polysulfides appear to be a less likely reaction product than iron coordinated persulfide species, which produce high intensity Raman bands below 253 cm⁻¹. The voltametric peaks A3 and C2 (Figure 2) could thus be mainly associated with disulfide species, although the equilibrium between the different chain lengths of polysulfides might have been altered during drying of the samples.

Thermodynamics of metal and ligand-based oxidation

Based on our results indicating initial formation of a ferric phase during FeS oxidation (Figure 1), we composed a potential energy surface of electronically unique, but stoichiometrically equivalent FeS models (Figure 7A). These models connect the postulated metal- and ligand-based intermediates and allow an initial assessment of possible states, which may preceded iron loss or sulfur addition during $n(Fe^{2+}S^{2-})_{(aq)}$ nanoparticle oxidation. The reference structure is the neutral [2Fe-2S] rhomb with antiferromagnetically coupled S=2 iron centers; a transient species formed during nucleation of mackinawite-like $n(Fe^{2+}S^{2-})_{(aq)}$ nanoparticles.[17] The [2Fe-2S] reference state can be represented by the (Fe 3d⁶⁺⁶/S 3p⁸⁺⁸) electron configuration. Upon 1e⁻ oxidation (bottom red arrow in Figure 7A), the rhomb converts to a mixed valence ferrous/ferric [2Fe-2S]⁺ paramagnetic ($S_t = 1/2$) state. The oxidation step is spontaneous by -12 kJ/mol (E° = +130 mV vs. Ag/AgCl). The second oxidation forms the diferric rhomb in a now endergonic step by 72 kJ/mol (E° = -308 mV). The 2e⁻ oxidized rhomb's electron configuration is (Fe 3d⁵⁺⁵/S 3p⁸⁺⁸), corresponding to metal-based oxidation. The latter two rhombs are the physiologically relevant forms of plant ferredoxins with comparable midpoint potentials (-340 to -500 mV).[63–65] The stability of protein bound diferric rhombs is due to the strong terminal L–M bond, which was not considered here for the sake of preserving the stoichiometry of intermediates throughout the entire potential energy surface.

Ligand-based oxidation cannot be directly accessed from the neutral, diamagnetic rhomb [2Fe-2S]. Instead, we constructed the chain model of a diferrous persulfide complex, [Fe-SS-Fe]²⁺ *trans* isomer shown in the bottom left of Figure 7A, which corresponds to the

electron configuration of (Fe $3d^{6+6}$/S $3p^{7+7}$). Unexpectedly, this pyrite mimic, without a ligand environment around the terminal ferrous centers and the persulfide anion, is only 35 kJ/mol (E° = -179 mV) higher than the reference [2Fe-2S] rhomb. The $1e^-$ reduction of the *trans* isomer (top blue arrow) leads to ligand-based redox changes, where the persulfide bond order is reduced and the S–S bond length in S_2^{3-} is elongated by 0.2 Å relative to S_2^{2-}. The paramagnetic [Fe-SS-Fe]$^+$ *trans* species is unstable (+142 kJ/mol and E° = -1.471 V) without the presence of a ligand environment around the terminal Fe^{2+} ions. An additional reduction step leads to complete dissociation and formation of two weakly interacting FeS diatomic molecules. These two FeS units can condense to form the initially discussed, neutral [2Fe-2S] rhomb. In line with this pathway, the literature examples showed that, during reductive dissolution of pyrite, the FeS unit containing mineral pyrrhotite (Fe$_{(1-x)}$S$_{(p)}$, where x < 0.17) is formed.[66]

In order to further explore the energy landscape and transitions between the pyrite mimic and mackinawite rhomb, including changes in the metal and ligand oxidation states, a plausible set of intermediates were generated by morphing the [2Fe-2S] rhomb and the [Fe-SS-Fe]$^{2+}$ chain. The morphing is along a coupled vibrational coordinate, where the two ferrous centers stretch in sync with the contraction of the S⋯S distance. The rhomb-to-chain morphing resulted in three unique intermediate structures, which are a lower energy [FeSFeS]$^+$ chain isomer, a [FeSSFe]$^+$ chain *cis* isomer, and a dissociated [FeS]+[FeS]$^+$ pair of diatomic molecules. The reverse, chain-to-rhomb morphing resulted only in two intermediates, which is a lower energy [Fe-SS-Fe]$^+$ *cis* isomer that is identical to the one found along the first morphing path ([FeSSFe]$^+$ chain *cis* isomer). The other isomer is very similar to the aforementioned [FeS]+[FeS]$^+$ pair. Thus, the energetic degeneracy of the [Fe-SS-Fe]$^+$ *cis* isomer and the [FeS]+[FeS]$^+$ pair offer a transition path between the metal- and ligand-based redox processes.

With the key isomers identified, we draw a potential pathway for connecting the metal- (right-hand side) and ligand (left-hand side of Figure 7A) based redox chemistry (Figure 7B). Starting from freshly precipitated n(Fe^{2+}S^{2-})$_{(s)}$, a one electron electrochemical oxidation results in Fe^{3+} containing rhombs and chain isomers (observable by XANES). The lower energy [FeSFeS]$^+$ chain isomer consists of multiple rotamers, which upon rotation of the common FeS bond, generates the [FeSSFe]$^+$ chain isomer leading to S-S bond formation and an intra-molecular redox shift, when the minimum distance between the sulfurs is reached (top right of Figure 7B). Following this change in the redox locus, a second one electron oxidation to a polysulfide containing species is indicated by new Raman vibrational modes ≤ 253cm^{-1}.

The free energy differences depicted in Figure 7A do not allow for a facile interconversion between the ligand-free, coordinatively unsaturated diiron persulfides and [2Fe-2S] rhombs under ambient conditions. However, when considering hydrothermal conditions, free energy differences of 100 kJ/mol can be readily overcome. Furthermore, addition of metal-terminal ligand bonds to the redox active moiety (to the dangling Fe^{2+} ions with $\Delta G_r°$ ~100 kJ/mol) or embedding the rhombs and chains into mineral/nanoparticle environment is expected to considerably decrease the free energy of

interconversion and thus flatten the potential energy surface. The metal- and ligand-based oxidation cycles may thus become energetically balanced, which provides the energetic rationale for the simultaneous presence of oxidized and reduced metals and ligands as seen in our experiments.

As ligand-based oxidation requires a structural rearrangement of two sulfide moieties (Figure 7, [2Fe-2S] rhomb → [FeSSFe]$^{2+}$ chain), metal-based oxidation likely occurs more readily, with the oxidation of iron preceding the oxidation of sulfide. Variability in the pathway energies could allow electrochemical promotion of these oxidation routes, altering the stoichiometry of x and y in Fe$^{2+}_{1-3x}$Fe$^{3+}_{2x}$S$^{2-}_{1-y}$(S$_n^{2-}$)$_y$. As the reduction of elemental sulfur (produced after the oxidation of polysulfides in A3 or their disproportionation) back to sulfide was observed in our voltametric experiments with n(Fe^{2+}S^{2-})$_{(s)}$ + Na$_2$S$_n$ in C2 (Figure 2b), the ligand-based oxidations appear to be reversible under the here investigated electrode potential ranges. The reduction of ferric iron to ferrous iron also appears to be feasible, as the electrode potentials necessary for the reduction of the ^{1}[2Fe-2S]$^{2+}$ / ^{2}[2Fe-2S]$^{1+}$ and ^{2}[2Fe-2S]$^{1+}$ / ^{1}[2Fe-2S]^0 redox couples are calculated to be -0.31 V and +0.13 V vs. Ag/AgCl, respectively. This would potentially permit the continuous cycling through the metal- and ligand-based oxidation states by avoiding the decomposition of the electrode through e.g. the accumulation of iron polysulfide species, making Fe$^{2+}_{1-3x}$Fe$^{3+}_{2x}$S$^{2-}_{1-y}$(S$_n^{2-}$)$_y$ suitable as an electrocatalyst.

Conclusions

We report the electrochemical synthesis of Fe^{3+} containing iron sulfide from freshly precipitated iron(II) sulfide under ambient conditions. Previously, temperatures above 70 °C and the addition of oxidants, such as FeCl$_3$ or H$_2$S, were necessary to accomplish this transformation.[21] The presence of ferric iron was indicated by a shift of the S K-edge XANES to lower energies from 2471 eV to 2470.2 eV and a Raman shift of the normal mode of n(Fe^{2+}S^{2-})$_{(s)}$ from 292 to 305 cm^{-1} at more positive electrode potentials. The production of polysulfides from Fe^{2+}S^{2-}$_{(s)}$ is detected in cyclic voltammograms due to the oxidation of polysulfides to elemental sulfur at 0 V. With increasing the applied electric potential from -0.8 V to -0.35 V and further to 0 V, n(Fe^{2+}S^{2-})$_{(s)}$ exhibited increases in the Raman signal intensities at 253 cm^{-1} and at wavenumbers below 140 cm^{-1}, which are attributed to a progression of the oxidation of sulfide to polysulfides. These vibrational modes are proposed to originate from iron bound persulfides, as shown on the core-extracted [2Fe-2S] in a persulfide ligand environment and model [2Fe-2S] persulfide clusters respectively.

Fe^{3+} and S_n^{2-} containing mackinawite is a chemically distinct FeS phase that exhibits both a ligand- and metal-centered redox locus, through the oxidation of sulfide to polysulfides and Fe^{2+} to Fe^{3+}. Its oxidized form is expressed here as Fe$^{2+}_{1-3x}$Fe$^{3+}_{2x}$S$^{2-}_{1-y}$(S$_n^{2-}$)$_y$ based on previous studies[33], estimating the Fe^{3+} content (x) to be less than 0.1. Within the scope of this work, we could not determine the amount of polysulfides (y) as an additional oxidation product. Analogous to the $2e^-$ redox reactions of the model [2Fe-2S] rhombs that mimic plant ferredoxins, n(Fe^{2+}S^{2-})$_{(s)}$ could potentially act as a catalyst for

reactions typically catalyzed by biological [Fe-S] clusters.[67] Further investigations into the reversibility of both Fe^{2+} and S^{2-} oxidation are necessary, but the reduction of elemental sulfur, produced during voltametric experiments from polysulfides, and the calculated redox potentials for $^{1}[2Fe\text{-}2S]^{2+}$ and $^{2}[2Fe\text{-}2S]^{1+}$ rhombs suggest the reversibility of these redox reactions. The presence of both ferric iron and polysulfides suggests that this material could potentially produce either $Fe^{2+}Fe_2^{3+}S_4^{2-}$ (greigite) or $Fe^{2+}S_2^{2-}$ (pyrite) based on the applied electrode potential. By understanding how solution and electrode potentials could favor either metal- or ligand-oxidation, tunability of these reaction routes can be achieved and the resulting material can be tailored towards facilitating reactions typically promoted by either greigite or pyrite.

Author Contributions

S.A.S., S.E.M. and R.K.Sz wrote the manuscript and conceptualized the presented work, S.A.S wrote the original manuscript, which was edited in initial rounds by R.K.Sz. and S.E.M.. S.A.S., S.E.M., R.K.Sz acquired, curated and validated the presented data. Y.L., N.K., S.M.W., T.Y assisted in the data acquisition and formal analysis. S.A.S., S.E.M., R.K.Sz, R.N, N.K. and S.M.W. developed the methodology concerning the data acquisition. Funding for this project and resources were acquired and supervision provided by S.E.M., R.K.Sz, and M.H.. All authors reviewed and edited this work prior to submission.

Conflicts of interest

There are no conflicts to declare.

Acknowledgements

Data Availability Statement

In order to accelerate this work and enhance the impact of our work, reference Raman and XANES spectra, as well as a full documentation of the computational results were uploaded online to a public depository Zenodo. The experimental data presented here is deposited under the following DOI: 10.5281/zenodo.5056738 and can be accessed via
https://zenodo.org/record/5056738

Notes and references

1 G. W. Luther, B. T. Glazer, L. Hohmann, J. I. Popp, M. Taillefert, T. F. Rozan, P. J. Brendel, S. M. Theberge and D. B. Nuzzio, *Journal of Environmental Monitoring*, 2001, **3**, 61–66.
2 R. A. Berner, *American Journal of Science*, 1970, **268**, 1–23.
3 M. S. Faber, M. A. Lukowski, Q. Ding, N. S. Kaiser and S. Jin, *J. Phys. Chem. C*, 2014, **118**, 21347–21356.
4 B. Konkena, K. junge Puring, I. Sinev, S. Piontek, O. Khavryuchenko, J. P. Dürholt, R. Schmid, H. Tüysüz, M. Muhler, W. Schuhmann and U.-P. Apfel, *Nature Communications*, 2016, **7**, 12269.
5 G. Wächtershäuser, *Systematic and Applied Microbiology*, 1988, **10**, 207–210.
6 W. Heinen and A. M. Lauwers, *Origins Life Evol Biosphere*, 1996, **26**, 131–150.
7 M. J. Russell and W. Martin, *Trends in Biochemical Sciences*, 2004, **29**, 358–363.
8 C. Huber and G. Wächtershäuser, *Science*, 1997, **276**, 245–247.
9 M. A. A. Schoonen, Y. Xu and J. Bebie, *Orig Life Evol Biosph*, 1999, **29**, 5–32.
10 M. Dörr, J. Käßbohrer, R. Grunert, G. Kreisel, W. A. Brand, R. A. Werner, H. Geilmann, C. Apfel, C. Robl and W. Weigand, *Angewandte Chemie International Edition*, 2003, **42**, 1540–1543.
11 A. D. Gordon, A. Smirnov, S. L. Shumlas, S. Singireddy, M. DeCesare, M. A. A. Schoonen and D. R. Strongin, *Orig Life Evol Biosph*, 2013, **43**, 305–322.
12 C. Bonfio, L. Valer, S. Scintilla, S. Shah, D. J. Evans, L. Jin, J. W. Szostak, D. D. Sasselov, J. D. Sutherland and S. S. Mansy, *Nature Chem*, 2017, **9**, 1229–1234.
13 N. Kitadai, R. Nakamura, M. Yamamoto, K. Takai, Y. Li, A. Yamaguchi, A. Gilbert, Y. Ueno, N. Yoshida and Y. Oono, *Science Advances*, 2018, **4**, eaao7265.
14 M. Preiner, K. Igarashi, K. B. Muchowska, M. Yu, S. J. Varma, K. Kleinermanns, M. K. Nobu, Y. Kamagata, H. Tüysüz, J. Moran and W. F. Martin, *Nat Ecol Evol*, 2020, **4**, 534–542.
15 R. Hudson, R. de Graaf, M. S. Rodin, A. Ohno, N. Lane, S. E. McGlynn, Y. M. A. Yamada, R. Nakamura, L. M. Barge, D. Braun and V. Sojo, *PNAS*, 2020, **117**, 22873–22879.
16 S. A. Sanden, R. Yi, M. Hara and S. E. McGlynn, *Chem. Commun.*, 2020, **56**, 11989–11992.
17 D. Rickard and G. W. Luther, *Chem. Rev.*, 2007, **107**, 514–562.
18 R. Guilbaud, I. B. Butler, R. M. Ellam and D. Rickard, *Earth and Planetary Science Letters*, 2010, **300**, 174–183.
19 G. W. Luther and D. T. Rickard, *J Nanopart Res*, 2005, **7**, 389–407.
20 A. Matamoros-Veloza, O. Cespedes, B. R. G. Johnson, T. M. Stawski, U. Terranova, N. H. de Leeuw and L. G. Benning, *Nature Communications*, 2018, **9**, 3125.
21 A. Roldan, N. Hollingsworth, A. Roffey, H.-U. Islam, J. B. M. Goodall, C. R. A. Catlow, J. A. Darr, W. Bras, G. Sankar, K. B. Holt, G. Hogarth and N. H. de Leeuw, *Chemical Communications*, 2015, **51**, 7501–7504.
22 S. Schouten, G. B. van Driel, J. S. Sinninghe Damsté and J. W. de Leeuw, *Geochimica et Cosmochimica Acta*, 1993, **57**, 5111–5116.
23 M. R. Raven, A. L. Sessions, J. F. Adkins and R. C. Thunell, *Geochimica et Cosmochimica Acta*, 2016, **190**, 175–190.
24 A. Picard, A. Gartman and P. R. Girguis, *Astrobiology*, , **21**(5), 587-604.
25 G. W. Luther, *Geochimica et Cosmochimica Acta*, 1991, **55**, 2839–2849.
26 D. T. Rickard, *Am J Sci*, 1975, **275**, 636–652.
27 A. R. Lennie, S. A. T. Redfern, P. E. Champness, C. P. Stoddart, P. F. Schofield and D. J. Vaughan, *American Mineralogist*, 1997, **82**, 302–309.
28 D. Rickard and G. W. Luther, *Geochimica et Cosmochimica Acta*, 1997, **61**, 135–147.
29 L. M. White, R. Bhartia, G. D. Stucky, I. Kanik and M. J. Russell, *Earth and Planetary Science Letters*, 2015, **430**, 105–114.
30 H. Wada, *BCSJ*, 1977, **50**, 2615–2617.
31 S. Boursiquot, M. Mullet, M. Abdelmoula, J.-M. Génin and J.-J. Ehrhardt, *Phys Chem Min*, 2001, **28**, 600–611.
32 J.-A. Bourdoiseau, M. Jeannin, R. Sabot, C. Rémazeilles and Ph. Refait, *Corrosion Science*, 2008, **50**, 3247–3255.
33 M. Mullet, S. Boursiquot, M. Abdelmoula, J.-M. Génin and J.-J. Ehrhardt, *Geochimica et Cosmochimica Acta*, 2002, **66**, 829–836.

ARTICLE

34   Y. Sano, A. Kyono, Y. Yoneda, N. Isaka, S. Takagi and G. Yamamoto, *Journal of Mineralogical and Petrological Sciences*, **115**, no. 3, 2020, 261–275.

35   J.-A. Bourdoiseau, M. Jeannin, C. Rémazeilles, R. Sabot and P. Refait, *Journal of Raman Spectroscopy*, 2011, **42**, 496–504.

36   D. Rickard, *Stockholm Contributions to Geology*, **20**, 67–95.

37   M. A. A. Schoonen and H. L. Barnes, *Geochimica et Cosmochimica Acta*, 1991, **55**, 1505–1514.

38   R. T. Wilkin and H. L. Barnes, *Geochimica et Cosmochimica Acta*, 1996, **60**, 4167–4179.

39   A. Kamyshny, A. Goifman, J. Gun, D. Rizkov and O. Lev, *Environ. Sci. Technol.*, 2004, **38**, 6633–6644.

40   S. M. Webb, *Physica Scripta*, 2005, **115**, 1011.

41   B. Ravel and M. Newville, *J Synchrotron Rad*, 2005, **12**, 537–541.

42   F. Weigend and R. Ahlrichs, *Phys. Chem. Chem. Phys.*, 2005, **7**, 3297–3305.

43   A. D. Becke, *Phys. Rev. A*, 1988, **38**, 3098–3100.

44   J. P. Perdew, *Phys. Rev. B*, 1986, **33**, 8822–8824.

45   M. J. Frisch, G. W. Trucks, H. B. Schlegel, G. E. Scuseria, M. A. Robb, J. R. Cheeseman, G. Scalmani, V. Barone, G. A. Petersson, H. Nakatsuji, X. Li, M. Caricato, A. V. Marenich, J. Bloino, B. G. Janesko, R. Gomperts, B. Mennucci, H. P. Hratchian, J. V. Ortiz, A. F. Izmaylov, J. L. Sonnenberg, D. Williams-Young, F. Ding, F. Lipparini, F. Egidi, J. Goings, B. Peng, A. Petrone, T. Henderson, D. Ranasinghe, V. G. Zakrzewski, J. Gao, N. Rega, G. Zheng, W. Liang, M. Hada, M. Ehara, K. Toyota, R. Fukuda, J. Hasegawa, M. Ishida, T. Nakajima, Y. Honda, O. Kitao, H. Nakai, T. Vreven, K. Throssell, J. A. Montgomery, Jr., J. E. Peralta, F. Ogliaro, M. J. Bearpark, J. J. Heyd, E. N. Brothers, K. N. Kudin, V. N. Staroverov, T. A. Keith, R. Kobayashi, J. Normand, K. Raghavachari, A. P. Rendell, J. C. Burant, S. S. Iyengar, J. Tomasi, M. Cossi, J. M. Millam, M. Klene, C. Adamo, R. Cammi, J. W. Ochterski, R. L. Martin, K. Morokuma, O. Farkas, J. B. Foresman, and D. J. Fox, *Gaussian 16, Revision C.01*, Wallingford CT, 2016, Gaussian, Inc.

46   A. V. Marenich, C. J. Cramer and D. G. Truhlar, *J. Phys. Chem. B*, 2009, **113**, 6378–6396.

47   F. L. Hirshfeld, *Theoret. Chim. Acta*, 1977, **44**, 129–138.

48   R. S. Mulliken, *J. Chem. Phys.*, 1955, **23**, 1833–1840.

49   D. Rickard, *Geochimica et Cosmochimica Acta*, 2006, **70**, 5779–5789.

50   A. J. Bard, R. Parsons and J. Jordan, *Standard Potentials in Aqueous Solution*, CRC Press, 1985.

51   A. N. Buckley, I. C. Hamilton and R. Woods, *Journal of Electroanalytical Chemistry and Interfacial Electrochemistry*, 1987, **216**, 213–227.

52   M. A. Aziz, M. Sohail, M. Oyama and W. Mahfoz, *Electroanalysis*, 2015, **27**, 1268–1275.

53   Y. Gorlin, A. Siebel, M. Piana, T. Huthwelker, H. Jha, G. Monsch, F. Kraus, H. A. Gasteiger and M. Tromp, *J. Electrochem. Soc.*, 2015, **162**, A1146.

54   T. A. Pascal, C. D. Pemmaraju and D. Prendergast, *Physical Chemistry Chemical Physics*, 2015, **17**, 7743–7753.

55   K. Rose Williams, B. Hedman, K. O. Hodgson and E. I. Solomon, *Inorganica Chimica Acta*, 1997, **263**, 315–321.

56   T. Glaser, K. Rose, S. E. Shadle, B. Hedman, K. O. Hodgson and E. I. Solomon, *J. Am. Chem. Soc.*, 2001, **123**, 442–454.

57   A. Baum, A. Milosavljević, N. Lazarević, M. M. Radonjić, B. Nikolić, M. Mitschek, Z. I. Maranloo, M. Šćepanović, M. Grujić-Brojčin, N. Stojilović, M. Opel, A. Wang, C. Petrovic, Z. V. Popović and R. Hackl, *Phys. Rev. B*, 2018, **97**, 054306.

58   P. L. Polavarapu, *J. Phys. Chem.*, 1990, **94**, 8106–8112.

59   D. Michalska and R. Wysokiński, *Chemical Physics Letters*, 2005, **403**, 211–217.

60   Y. E. Mendili, B. Minisini, A. Abdelouas and J.-F. Bardeau, *RSC Advances*, 2014, **4**, 25827–25834.

61   D. Coucouvanis, D. Swenson, P. Stremple and N. C. Baenziger, *J. Am. Chem. Soc.*, 1979, **101**, 3392–3394.

62   G. J. Janz, J. W. Coutts, J. R. Downey and E. Roduner, *Inorg. Chem.*, 1976, **15**, 1755–1759.

63   W. Buckel and R. K. Thauer, *Front Microbiol*, **9** (2018): 401.

64   B. Li and S. J. Elliott, *Electrochimica Acta*, 2016, **199**, 349–356.

65   W. Thamer, I. Cirpus, M. Hans, A. J. Pierik, T. Selmer, E. Bill, D. Linder and W. Buckel, *Arch Microbiol*, 2003, **179**, 197–204.

66   J. M. Lambert, G. Simkovich and P. L. Walker, *Fuel*, 1980, **59**, 687–690.

67   H. Beinert, R. H. Holm and E. Münck, *Science*, 1997, **277**, 653–659.